

Comparison of McMaster Nuclear Reactor Irradiation Experiments with Simulation

John A. Kennedy, Simon E. Day

McMaster University
Dept. of Engineering Physics JHE/A235
1280 Main Street West
Hamilton, Ontario
L8S 4L7
Supervisor: Dr. Wm. J. Garland

Abstract

A detailed series of irradiation experiments were conducted in the McMaster Nuclear Reactor (MNR), a 2 MW_{th}, light-water moderated, pool-type research reactor, between March 1997 and January 1999.

Standard radioactivation techniques were used to determine the experimental reaction rates of combinations of eight nuclear reactions in seven different core configurations. The reactions used in this study were: $^{55}\text{Mn}(n,\gamma)^{56}\text{Mn}$, $^{58}\text{Fe}(n,\gamma)^{59}\text{Fe}$, $^{59}\text{Co}(n,\gamma)^{60}\text{Co}$, $^{63}\text{Cu}(n,\gamma)^{64}\text{Cu}$, $^{115}\text{In}(n,\gamma)^{116}\text{In}$, $^{197}\text{Au}(n,\gamma)^{198}\text{Au}$, $^{27}\text{Al}(n,\alpha)^{24}\text{Na}$, and $^{115}\text{In}(n,n')^{115}\text{In}^*$.

The irradiations were performed in the Central Irradiation Facility (CIF), the in-core ^{125}I production sites and the graphite reflector, and included both unshielded and Cd-shielded cases. For the iodine and graphite sites, axial maps of $^{59}\text{Co}(n,\gamma)$ and $^{27}\text{Al}(n,\alpha)$ reaction rates were experimentally determined for three core configurations.

Reaction rates were compared to calculated values produced from simulation using the WIMS-AECL/3DDT code package.^(1,2) In addition, a neutron flux spectrum unfolding code, SAND-II,⁽³⁾ was used to generate flux spectra from the experimental results for comparison with the WIMS-AECL/3DDT flux spectra.

Good agreement between experimental and calculated results were found in the majority of the Co/Al wire cases. The suitability of different foil materials and methodologies are identified.

1.0 Introduction

MNR is a 2 MW_{th}, light-water moderated, pool-type research reactor composed of plate-type fuel. A detailed series of irradiation experiments were conducted between March 1997 and January 1999.

The core is defined by a 9 × 6 site grid plate with an active axial height of 60 cm. Each core site is roughly 8 cm by 8 cm. The core is divided into 6 columns: A to F; and 9 rows: 1 to 9. Figure 1 shows the layout of one of the 7 core configurations studied.

The irradiations were performed in the CIF (Site 5c), the in-core ^{125}I production sites, and the graphite reflector. The CIF is a high neutron flux site ($\sim 5 \times 10^{13}$ n/cm²/s thermal flux) and the row 8 sites contain graphite reflector assemblies that are hollowed, allowing the placement of samples in an area of mostly thermal neutron flux ($\sim 1 \times 10^{13}$ n/cm²/s thermal flux). Samples were generally placed at the axial midpoint of the sites.

For core configuration 48I, in Site 8d, samples of unshielded Co/Al wire were spaced

	A	B	C	D	E	F
1	water	water	fuel	fuel	fuel	fuel
2	beryllium reflector	fuel	fuel (shim rod)	fuel	fuel (shim rod)	fuel
3	fuel	fuel	fuel	fuel	fuel	fuel
4	fuel	fuel (shim rod)	fuel	fuel	fuel (shim rod)	fuel
5	fuel	fuel	water	fuel	fuel	fuel
6	fuel	fuel (shim rod)	fuel	fuel	fuel (regulating rod)	fuel
7	water	fuel	fuel	fuel	fuel	graphite
8	graphite	graphite	graphite	graphite	graphite	graphite
9	water	water	water	graphite	water	water

Figure 1: MNR Core 48E

along a sample tube at 2.5, 18.2, 33.9, 48.7, and 59.5 cm from its bottom.

More detailed axial mappings were done for core configuration 48M sites 7c and 8f, and core configuration 49A sites 7c and 7f. These sites are of interest in ^{125}I production.

Details of the arrangement of the experiment are given in Section 2.0.

Calculations of reaction rates were performed according to ASTM standards.^(4,5)

Estimates of the reaction rates due to thermal flux were made by repeating foil activations with cadmium shielding. ASTM standards provide average cross sections and resonant integrals to estimate thermal, epi-thermal and fast neutron flux from experimental reaction rates. However, reaction rates, not flux estimates, were used for most comparisons because methods which convert experimental reaction rates into flux data require assumptions about cross sections and the shape of the neutron flux spectrum. ASTM calculations are described in Section 3.0.

The foil experiments were modelled using the WIMS-AECL/3DDT code package^(1,2) to produce microscopic cross sections, reaction rates, and 8-group core flux spectra. The foil experiment geometries were incorporated into the transport theory cell models, which, in turn, provided cross section input data for the whole-core diffusion theory models. The fluxes were used to calculate theoretical reaction rates for the foils. The simulation analysis is described in detail in Section 4.0.

A comparison of experimental and modelled reaction rate results is discussed in Section 5.0.

A neutron flux spectrum unfolding code, SAND-II,⁽³⁾ was used to generate flux spectra from the experimental results for comparison with the modelled flux spectra. The SAND-II code is intended to determine neutron energy spectra by an analysis of activated foil data. The code is designed to provide a “best fit” neutron flux spectrum for a given input set of foil reaction rates. By calculating the foils’ reaction rates from a library of cross sections, and adjusting the flux spectrum in an iterative process, the code attempts to match the experimental results. The version used requires that foils sensitive to thermal and epi-thermal neutrons must have at least one bare and one covered reaction rate as inputs. Details of the SAND-II code are given in Section 6.0 and the limitations of flux estimates are discussed in Section 7.0.

Figure 2: Experimental Estimation of MNR Neutron Flux

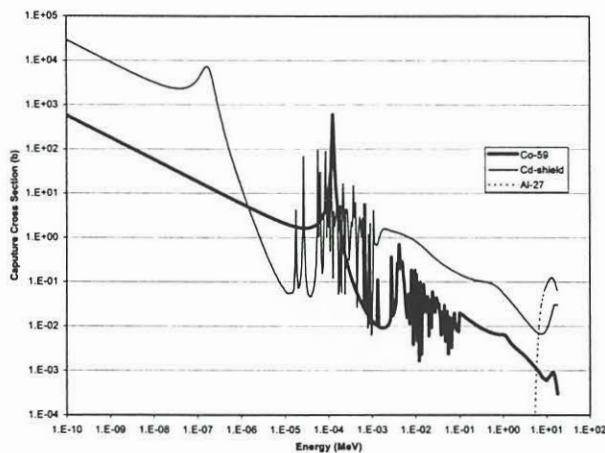
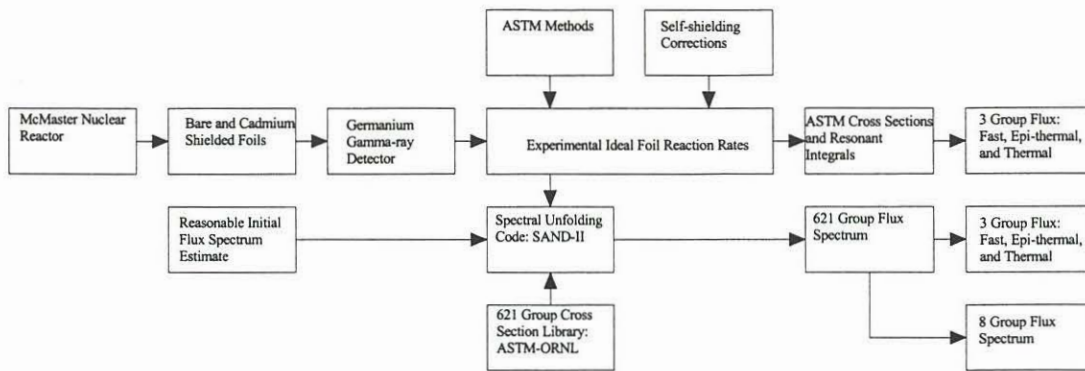


Figure 3: Microscopic Cross Sections

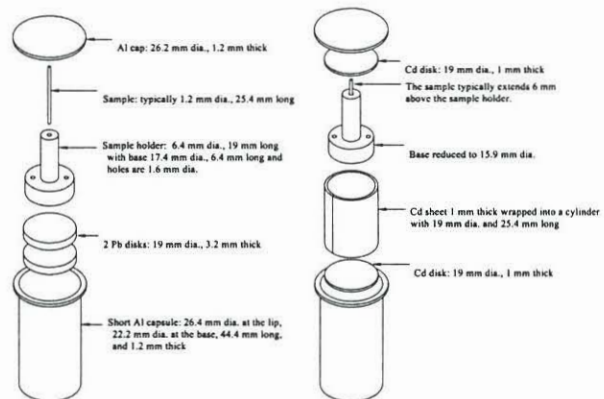


Figure 4: Aluminum Capsules for Foils

2.0 Experiment

Figure 2 shows two methods of estimating an energy dependent neutron flux spectrum of MNR by experiment: ASTM calculations and a SAND-II spectrum unfolding method.

In the ASTM-based method,^(4,5) “foils” (wires) were activated in the reactor core. Foils were chosen for their sensitivity to thermal and epi-thermal (resonance) neutron flux. These foils were: ^{55}Mn , ^{58}Fe , ^{59}Co , ^{63}Cu , ^{115}In , and ^{197}Au . They all undergo an (n,γ) reaction. An estimate of the thermal flux can be made by repeating foil activation with cadmium shielding. Fast flux estimates can be made by $^{27}\text{Al}(n,\alpha)^{24}\text{Na}$, and $^{115}\text{In}(n,n')^{115}\text{In}^*$ reactions. ASTM standards provide average cross sections and resonance integrals to estimate thermal, epi-thermal and fast neutron flux from experimental reaction rates. However, in order to make the fewest assumptions about cross sections for the experimental results, reaction rates were chosen as a basis of comparison between experiment and simulation.

Standard foils have reactions which occur over a broad range of neutron energies, quantified by energy dependent microscopic cross sections. Often materials with high thermal

cross sections have significant resonances in the epi-thermal range. A thin (1 mm) cadmium shield was used to remove the thermal neutrons from some samples so that the effects of thermal and epi-thermal neutrons could be separated. Figure 3 shows that Cd has a cross section that is over 10 times that of the thermal detector foil, cobalt, below the thermal cut-off energy (typically 0.625 eV).⁽⁶⁾ The resonances of the foil materials used as fast neutron detectors (e.g., aluminum) are relatively insignificant.

Sample wires were typically 25 mm long and 1 mm in diameter. Each wire was placed, in turn, in an aluminum stand to hold it vertical. The wire and stand were then placed in a standard short aluminum capsule (see Figure 4). A cadmium lining was cut to fit the inside of the capsules. For those capsules without Cd lining, two lead discs were cut to fit in the bottom to prevent the sealed capsule from floating to the top of the sample tube when placed in the irradiation site. The sample tube was a hollow 80 cm Al tube, about 3 cm in diameter (see Figure 5). The tube was loaded from the top of the reactor and had collar which centred the tube in the middle of the site. Solid Al spacers raised the point at which the sample rested to the axial midpoint of the reactor core.

For detailed axial mappings of Core 48M sites 7c and 8f, and Core 49A sites 7c and 7f, Co/Al wires were aligned along the compass points of the interior of a RIFLS (Reactor Irradiation Facility for Large Samples) tube. A RIFLS tube is a hollow 6 cm diameter aluminum tube, about 75 cm long, weighted at the bottom with about 17 cm of lead.⁽⁷⁾ Shielded tubes are lined with about 1 mm of Cd. The bottom of a RIFLS tube interior is roughly 35 cm from the bottom of the reactor grid plate. For each of the two core configurations, Co/Al wire cages were constructed (see Figure 6). The four 50 cm edges were scored every inch (2.54 cm) to facilitate

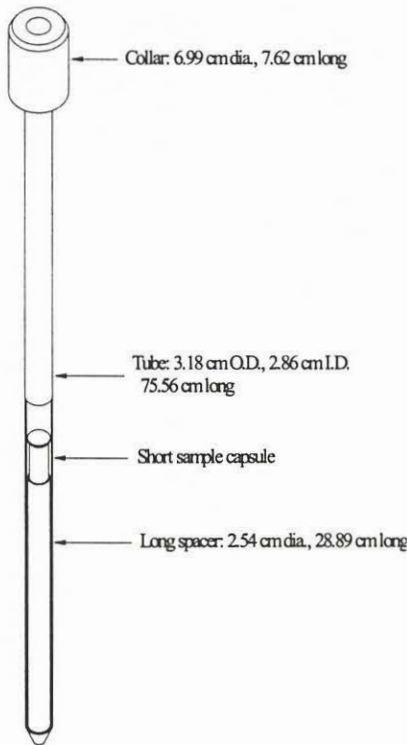


Figure 5: Sample Tube

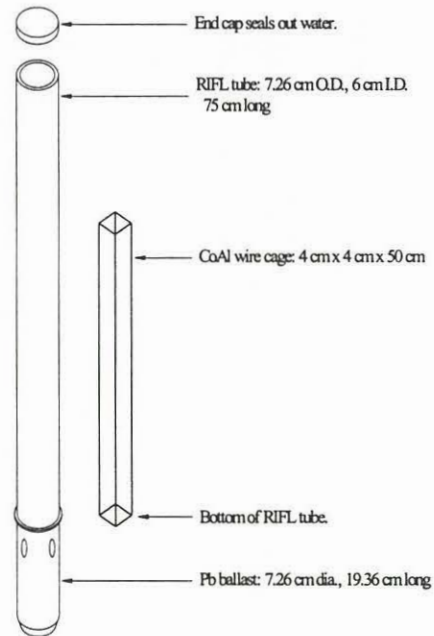


Figure 6: RIFLS Tube

cutting after irradiation. The cages were placed at the bottom of the RIFLS tube which was then capped. For both cores, two unlined RIFLS tubes were inserted into the core in the pair of sites of interest for one hour. These were removed and immediately replaced by two Cd-lined RIFLS tubes. A day after irradiation, the cages were removed and cut along the axis every inch. This generated about 320 samples per core to be counted.

To obtain absolute measurements of foil activity, the efficiencies of a gamma detector

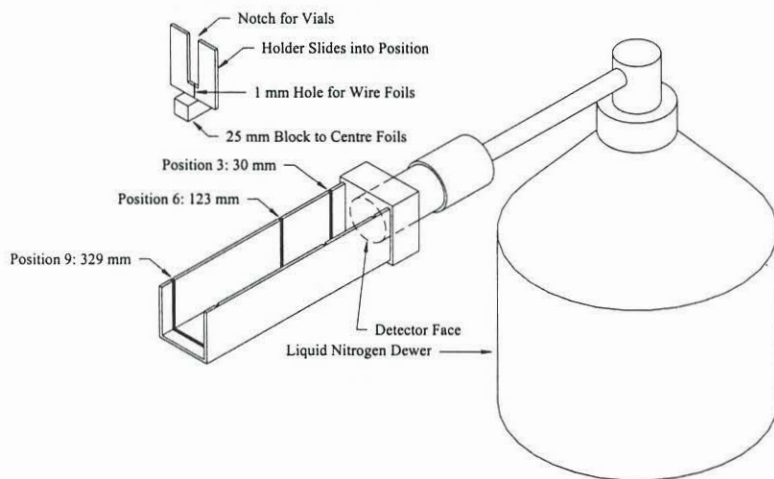


Figure 7: Ge Detector

were determined. An n-type high-purity germanium coaxial photon detector was used for counting. The detector signal was processed through a preamplifier, an amplifier, and a 4K multichannel analyzer. Peak definition, peak counts, the subtraction of background counts, dead time, and count error were calculated by ApteC PCMCA/WIN software.⁽⁸⁾ The peaks of interest were well defined and fell in the range of 336.2 keV to 1507.4 keV.

Samples were placed in Lucite holders which centred them along the axis of the detector. To minimize dead time, positions 30 mm, 123 mm, and 329 mm from the detector face were used, depending on sample activity. Figure 7 shows the relationship between the sample position and the detector.

The certified standard sources used for absolute calibration of the detector were ¹⁵²Eu, ¹⁵⁴Eu, ¹³³Ba, ⁶⁰Co, and ²²Na. These provided 24 gamma energy peaks ranging in energy from 276.39 keV to 1596.50 keV. The efficiency (ϵ) of the detector for each peak was found from:

$$\epsilon = \frac{C_a}{A_0 I_\gamma \exp(-\lambda t)} \quad , \quad \lambda = \frac{\ln(2)}{t_{1/2}} \quad (1)$$

where the numerator (C_a) was the actual count rate and the denominator was the count rate to be expected if all the events were counted. The activity at the time of certification (A_0) was modified by the decay constant (λ) considering the time elapsed (t); and also by the peak yield (I_γ): the fraction of gamma rays produced at the energy of interest for each disintegration. The decay constant is usually listed in terms of the isotope's half-life ($t_{1/2}$).

It is not uncommon to least-square fit a fourth or fifth order polynomial to the efficiencies determined by the standard sources.⁽⁹⁾ A fourth order polynomial in energy (E) was used to fit the efficiency (ϵ) in positions 6 and 9. Figure 8 shows the fitted efficiency curve for position 6. The curve for position 9 was similar in shape. For position 3 a linear fit of the detector efficiency was used. Position 3 was used for the cobalt and aluminum foils of the axial

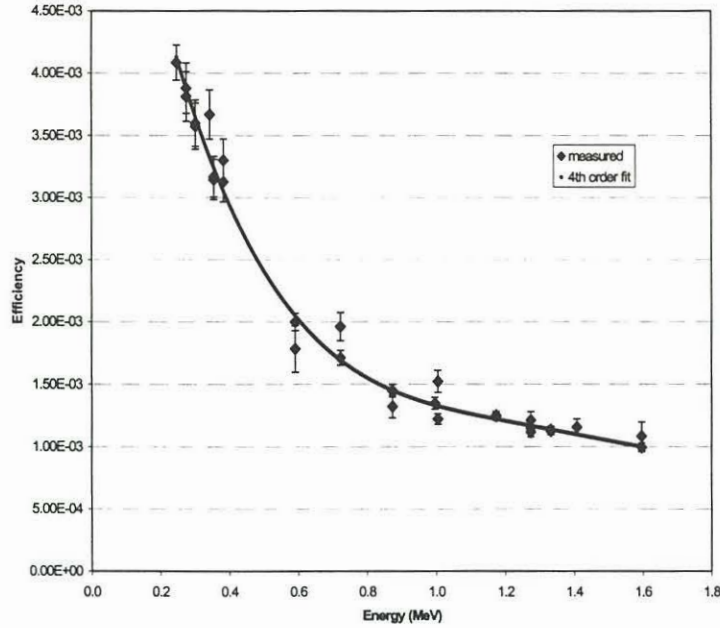


Figure 8: Detector Efficiency Curve for Position 6

3.0 ASTM Calculations

Calculations of reaction rates were performed according to ASTM standards.^(4,5) According to this method, the reaction rate is the saturated activity calculated per parent nuclide. The saturated activity is defined as the activity if the sample is left in the reactor until the isotope production rate equals the decay rate. The reaction rate (R_s) is given by:

$$R_s = \frac{C_T}{\epsilon I_\gamma N_0} \frac{\lambda \exp(\lambda t_w)}{(1 - \exp(-\lambda t_c))(1 - \exp(-\lambda t_i))} , \quad N_0 = N_A f P m / w \quad (2)$$

where C_T is the actual count which is divided by the detector efficiency and the peak yield to give the total disintegrations per second of the sample. The waiting time is t_w and the counting time is t_c . The number of parent nuclei in the sample (N_0) are assumed not to change significantly during the irradiation time (t_i) and is given in terms of Avogadro's number (N_A), the fraction of the sample containing the element of the foil (f), the weight percent (as a fraction) of the isotope compared to the parent element (P), the mass of the sample (m), and the molecular weight of the parent element (w). Strictly speaking the method alters the reaction rate and the irradiation time by a factor λ'/λ which accounts for the removal by transmutation of some of the daughter nuclei. Although this could be easily estimated for cobalt, copper, and gold foils, it added less than 0.1 % to any of the reaction rates.

The ASTM standard⁽⁵⁾ recommends that reaction rates be corrected to the ideal case of infinite dilution. This was significant for gold, indium, and, to some extent, cobalt foils. Estimates were made to remove the effect in which the interior of the sample was shielded by the material toward the sample surface. The self-shielding factor (G) can be expressed as the ratio of the average flux experienced throughout the foil ($\bar{\phi}$) to the actual flux at the foil surface (ϕ_0):

$$G = \bar{\phi} / \phi_0 \quad (3)$$

Self-shielding factors are listed for thermal (G_{th}) and resonance energies (G_{res}). Reaction rates

mapping experiments. The ^{60}Co and ^{22}Na sources provided efficiency measurements at 1173.24, 1274.53, and 1332.50 keV.

The foil samples were placed in the MNR core for times ranging from 6 minutes to 10 hours. After removal, samples were allowed to "cool" for 1 to 14 days to facilitate counting. Depending on sample activity, counting times varied between 20 s and 100 minutes.

are proportional to flux, so the measured reaction rates are proportional to the self-shielding factor and the cases of infinite dilution were calculated as:

$$R_{\infty,th} = R_{s,th} / gG_{th} \quad , \quad R_{\infty,Cd} = R_{s,Cd} / G_{res} \quad (4)$$

where $R_{s,th}$ and $R_{s,Cd}$ are the components of the reaction rates due to thermal and epi-thermal neutrons respectively, and $R_{\infty,th}$ and $R_{\infty,Cd}$ are their ideal, infinite dilution counterparts. The Wescott g factor “is a correction factor that accounts for the departures from the ideal $1/v$ detector cross section in the thermal energy range”⁽⁵⁾ and reduced the thermal reaction rate by less than 2 % for indium, 0.5 % for gold, and did not affect cobalt calculations.

Since the thermal component of the reaction rate was estimated by the difference between the reaction rates obtained by bare ($R_{s,bare}$) and cadmium-shielded foils ($R_{s,Cd}$), the total infinite dilution reaction rate for indium, gold, and cobalt samples was found from:

$$R_s = \left(R_{s,bare} - R_{s,Cd} \right) / gG_{th} + R_{s,Cd} / G_{res} \quad (5)$$

Tables are available⁽⁵⁾ listing G_{th} and G_{res} for 1 % cobalt/aluminum wire (0.99 and 0.96 respectively). A log-log extrapolation of the G_{res} table for gold wire gave 0.158, but there were no data for G_{th} for gold so it was set to unity.

The self-shielding data table for indium only gave values for foils (slabs) not wires. A log-log extrapolation was done to extend the table to the thickness of the indium wires used. A correction factor for converting slab to wire values was derived by comparing a power series solution of the diffusion equation for cylindrical geometry to the solution for a slab geometry. Values for indium of 0.658 and 0.157 were used for G_{th} and G_{res} , respectively.

4.0 Simulation

Reaction rates were also produced from simulation using the WIMS-AECL/3DDT code package.^(1,2) Here, an absolute reaction rate or flux value in a sub-domain of a given cell is of interest, so a “fine structure” (or microscopic) analysis using the transport theory code was coupled to a macroscopic solution which was provided by a diffusion theory code. The two solutions complement each other.

“Fine Structure” refers to the detailed geometry of a given section of the system under investigation. Typically this geometric detail includes material heterogeneities over small distances (*e.g.*, adjacent absorber, void, and moderator regions) and must be analyzed using a transport theory code, as diffusion theory is invalid in such circumstances.

The transport theory solution provides the flux spectrum for the region of interest within the cell in question (*e.g.*, the central irradiation region within a graphite assembly) as well as a cell-averaged flux spectrum. These transport theory solutions are often given an arbitrary normalization (*e.g.*, 1 cell absorption). In contrast, the diffusion theory solution provides a similar cell-averaged flux spectrum, which has been normalized to the nominal power level.

Assuming that the transport theory cell model is a good representation of the corresponding cell in the core solution, the transport theory and diffusion theory cell-averaged flux solutions should differ only in their magnitudes. With this assumption, the ratio of the regional to cell-averaged integrated flux from the transport theory solution should be identical to the same ratio from the diffusion theory solution, *i.e.*,

$$\frac{\phi_{transport}^{region_i}}{\phi_{transport}^{cell-averaged}} = \frac{\phi_{diffusion}^{region_i}}{\phi_{diffusion}^{cell-averaged}} \quad (6)$$

These relations allow the regional flux spectra from the transport theory solution to be “re-normalized” to be consistent with the diffusion theory solution magnitude. This operation can be thought of as either: (a) re-normalizing the regional flux spectra using the ratio of the transport theory to diffusion theory cell-averaged fluxes, or (b) extracting the normalized regional flux spectra from the core flux distribution using the fine-structure flux ratios. These concepts are shown below with the diffusion theory solution re-named “absolute” and the transport theory solution re-named “micro” with regards to the normalization:

$$\begin{aligned} \phi_{absolute}^{region_i} &= \phi_{micro}^{region_i} \times \text{Re - Normalization Factor} \\ &= \phi_{micro}^{region_i} \times \left\{ \frac{\phi_{absolute}^{cell-averaged}}{\phi_{micro}^{cell-averaged}} \right\} \end{aligned} \quad (7)$$

Or,

$$\begin{aligned} \phi_{absolute}^{region_i} &= \phi_{absolute}^{cell-averaged} \times \text{Fine - Structure Ratio} \\ &= \phi_{absolute}^{cell-averaged} \times \left\{ \frac{\phi_{micro}^{region_i}}{\phi_{micro}^{cell-averaged}} \right\} \end{aligned} \quad (8)$$

In practice, it is usually easier to form fine-structure flux ratios from the regional and cell-averaged transport theory fluxes. These ratios are then “applied” to the corresponding cell-averaged quantities found from the diffusion solution. In this way, the data from the transport theory solution can be handled separately from that from the diffusion theory solution until the final calculation step.

An example of the sort of calculation scheme used in this analysis is shown in Figure 9.

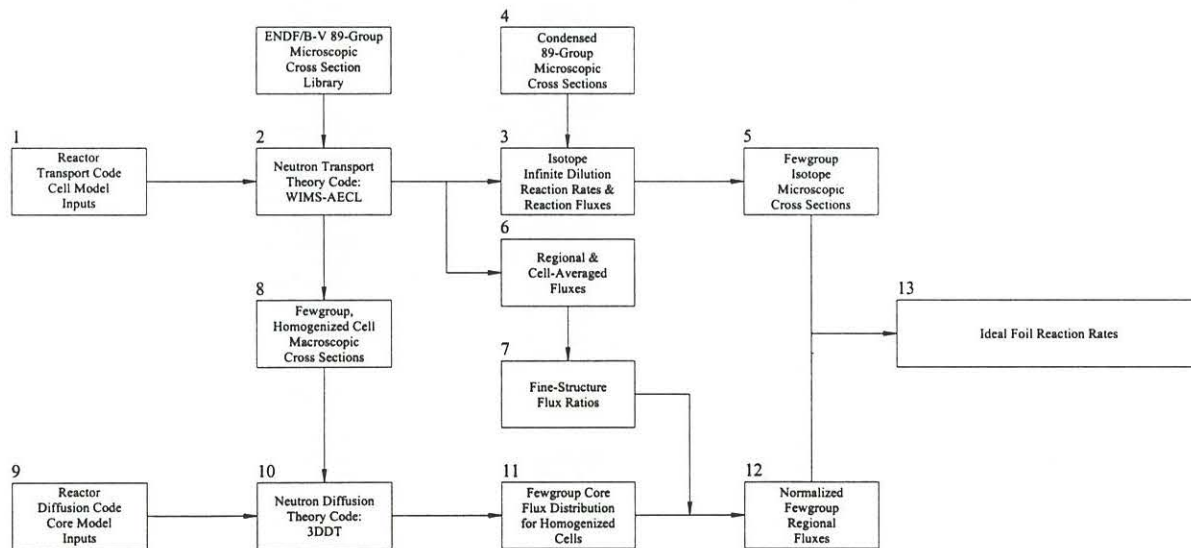


Figure 9: Calculation Scheme for Simulation of Foil Experiments

The various stages are described below:

1. The experimental irradiation set up was included in the appropriate transport theory cell model (note: the actual foil materials were not included in the model). The desired foil isotope reaction rates were specified in the transport theory model input for the sub-domain of the cell (*i.e.*, where the foil would be located in the irradiation set up). This approach assumed that the presence of the foils do not significantly perturb the flux solution.
2. The transport theory cell model was executed, using the appropriate microscopic cross section library; *i.e.*, an ENDF/B-V based WIMS-AECL library with cross sections in an 89-group energy structure. Included in the output were the infinite-dilution isotopic reaction rates (3), the regional and cell-averaged fluxes (6), and the appropriate few-group cell-averaged cross sections for use in the companion diffusion code model (8).
3. The infinite dilution isotopic reaction rates were extracted from the transport theory model output along with the corresponding regional flux spectra. The corresponding microscopic cross sections were then calculated from the reaction rates and flux data for the isotopes of interest.
4. Some reaction cross sections relevant to the foil irradiation experiments in MNR are not included in the WIMS-AECL library (*e.g.*, $^{27}\text{Al}(n,\alpha)^{24}\text{Na}$, $^{58}\text{Fe}(n,\gamma)^{59}\text{Fe}$, and $^{115}\text{In}(n,n')^{115}\text{In}^*$). These cross sections were extracted from an ASTM-ORNL library used with the SAND-II flux unfolding code and are given in 621 energy groups. The 621-group data were condensed, using a crude spectrum approximation (*i.e.*, a Maxwell-Boltzman thermal distribution, a 1/E epithermal distribution and a fission spectrum fast distribution), to the WIMS-AECL library 89-group structure.
5. The isotope microscopic cross sections, from steps (3) and (4) were condensed, using the applicable transport-theory-solution regional flux spectra, to the same few-group structure as the diffusion theory flux solution.
6. The regional and cell-averaged integrated flux spectra were extracted from the transport theory model output. The consistency of the regional and cell-averaged flux spectra, in terms of reaction rates, was checked at this point.
7. The transport theory solution regional and cell-averaged integrated fluxes were used to determine the region to cell-averaged flux ratios for the region of interest (*e.g.*, the region where the foil irradiations took place).
8. The appropriate few-group cell-averaged macroscopic cross sections for use in the companion diffusion theory model were extracted from the transport theory model output.
9. The companion diffusion theory model input file was created, referencing the cell-averaged cross section data from the transport theory model output.
10. The diffusion theory model was executed. The output gives a few-group flux distribution for the core, based on homogenized cell zones. The flux distribution is normalized to the nominal core power.
11. The few-group, cell-averaged flux distribution was extracted from the diffusion theory model output.
12. The transport theory model region to cell-averaged flux ratios and the diffusion theory solution cell-averaged fluxes were used to determine the absolute (*i.e.*, normalized to core power) region flux for the region of interest.
13. The few-group isotope microscopic cross sections from (5) and the normalized few-group region fluxes from (12) were used to calculate the infinite dilution (or ideal) foil reaction rates.

Table 1: Experimental and Simulated Reaction Rates for Cores 48E through 48I.

Parent Element	Reactor Core	Site	Cadmium Shielded?	Experimental Reaction Rate (s ⁻¹)	Error in Experimental Reaction Rate	Simulated Reaction Rate (s ⁻¹)	Percent Difference between Simulated and Experimental Rates
aluminum	48E	5c	no	8.20E-15	2.9%	8.34E-15	1.6%
aluminum	48E	5c	yes	7.57E-15	1.7%	8.26E-15	9.1%
cobalt	48E	5c	no	1.59E-09	2.3%	1.55E-09	-2.1%
cobalt	48E	5c	yes	1.05E-10	1.8%	9.78E-11	-7.2%
aluminum	48E	8d	no	2.01E-15	2.5%	1.94E-15	-3.5%
cobalt	48E	8d	no	4.79E-10	2.4%	4.81E-10	0.4%
cobalt	48E	8d	no	4.86E-10	2.3%	4.81E-10	-1.1%
aluminum	48F	8d	no	1.92E-15	3.9%	1.79E-15	-6.6%
aluminum	48F	8d	yes	2.04E-15	4.5%	1.78E-15	-12.8%
cobalt	48F	8d	no	4.84E-10	4.2%	4.48E-10	-7.5%
cobalt	48F	8d	yes	2.95E-11	2.3%	2.94E-11	-0.5%
copper	48F	8d	no	8.70E-11	28.2%	5.28E-11	-39.3%
copper	48F	8d	yes	1.85E-12	31.0%	2.30E-12	24.6%
gold	48F	8d	no	3.06E-09	10.1%	1.73E-09	-43.4%
gold	48F	8d	yes	2.62E-09	10.1%	6.07E-10	-76.9%
indium	48F	8d	no	2.59E-09	17.5%	3.03E-09	17.0%
indium	48F	8d	yes	7.84E-10	17.6%	1.06E-09	35.7%
indium n,n'	48F	8d	no	5.49E-13	17.4%	6.14E-13	11.8%
indium n,n'	48F	8d	yes	5.86E-13	17.4%	6.07E-13	3.5%
iron	48F	8d	no	1.62E-11	6.4%	1.54E-11	-4.8%
iron	48F	8d	yes	5.47E-13	8.1%	6.74E-13	23.3%
manganese	48F	8d	yes	4.73E-12	16.7%	5.75E-12	21.5%
aluminum	48G	5c	no	8.86E-15	2.6%	8.07E-15	-8.9%
aluminum	48G	5c	no	7.94E-15	2.3%	8.07E-15	1.7%
aluminum	48G	5c	yes	7.82E-15	2.3%	8.00E-15	2.2%
cobalt	48G	5c	no	1.56E-09	2.0%	1.52E-09	-2.6%
cobalt	48G	5c	no	1.59E-09	2.2%	1.52E-09	-4.3%
cobalt	48G	5c	yes	1.04E-10	2.9%	9.56E-11	-8.0%
copper	48G	5c	no	1.75E-10	3.4%	1.80E-10	2.8%
copper	48G	5c	yes	6.44E-12	6.2%	7.48E-12	16.1%
gold	48G	5c	no	3.30E-09	3.8%	5.85E-09	77.5%
gold	48G	5c	yes	1.47E-09	3.8%	2.00E-09	36.2%
indium	48G	5c	no	9.44E-09	8.3%	1.02E-08	8.6%
indium	48G	5c	yes	2.60E-09	8.6%	3.51E-09	34.8%
indium n,n'	48G	5c	no	2.19E-12	7.2%	2.41E-12	9.8%
indium n,n'	48G	5c	yes	2.11E-12	7.2%	2.37E-12	12.7%
manganese	48G	5c	no	3.78E-10	6.4%	5.27E-10	39.5%
manganese	48G	5c	yes	1.40E-11	5.4%	1.88E-11	34.3%
copper	48G	8d	no	5.10E-11	4.3%	5.26E-11	3.2%
manganese	48G	8d	no	1.43E-10	4.0%	1.54E-10	8.0%
copper	48H	8d	yes	1.82E-12	5.8%	2.77E-12	52.3%
gold	48H	8d	no	1.23E-09	3.8%	2.08E-09	69.5%
gold	48H	8d	yes	4.91E-10	3.8%	7.31E-10	49.0%
indium	48H	8d	no	3.38E-09	7.3%	3.65E-09	7.7%
indium	48H	8d	yes	1.24E-09	7.4%	1.28E-09	3.2%
indium n,n'	48H	8d	no	6.04E-13	6.2%	7.39E-13	22.5%
indium n,n'	48H	8d	yes	6.48E-13	6.2%	7.33E-13	13.1%
manganese	48H	8d	yes	4.48E-12	4.0%	6.93E-12	54.7%
gold	48I	5c	yes	1.68E-09	3.8%	2.04E-09	21.7%
iron	48I	5c	no	6.54E-11	5.1%	5.37E-11	-17.9%
iron	48I	5c	yes	2.19E-12	5.4%	2.24E-12	2.2%
indium	48I	8d	no	2.80E-09	6.9%	3.25E-09	16.3%
indium n,n'	48I	8d	no	5.37E-13	5.5%	6.57E-13	22.4%
iron	48I	8d	no	1.63E-11	5.1%	1.66E-11	1.7%
iron	48I	8d	yes	6.52E-12	5.0%	7.23E-13	-88.9%

5.0 Comparison of Results

Table 1 lists the experimental and simulated reaction rates. Over half of the simulated reaction rates have a difference of greater than 10 % when compared to the experimental values. However, only 14 of these 55 trials were different by more than 25 %. The experimental reaction rate of the cadmium shielded iron sample in Core 48I Site 8d is almost an order of magnitude larger than a similar sample in a similar core in the same site: Core 48F Site 8d. Also, unexpectedly, it has an activity almost 3 times larger than a similar sample in the centre of the reactor (Core 48I Site 5c). This suggests a procedural error in the measurement of that sample, rather than large error in the simulation's calculation. This sample gives the largest difference when compared to the simulation (-88.9 %). Of the 55 trials, 17 simulation calculations fall within the experimental error. The most consistent results are given by aluminum (a fast neutron detector) and cobalt (a thermal and epi-thermal neutron detector).

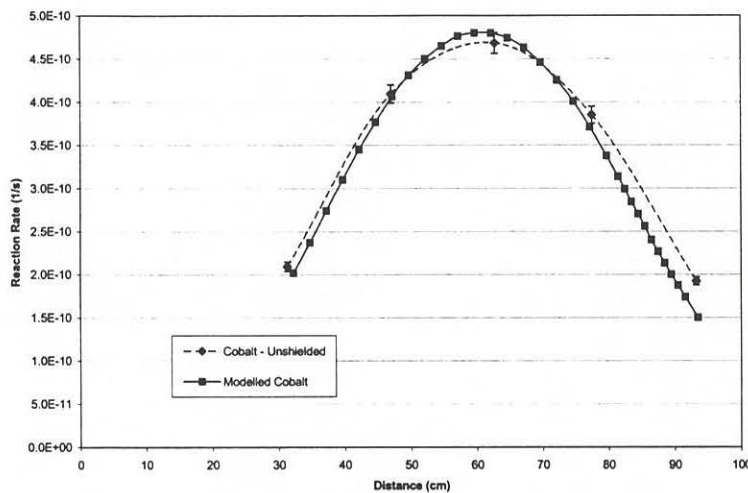


Figure 10: Core 48I Axial Reaction Rates of Bare Cobalt

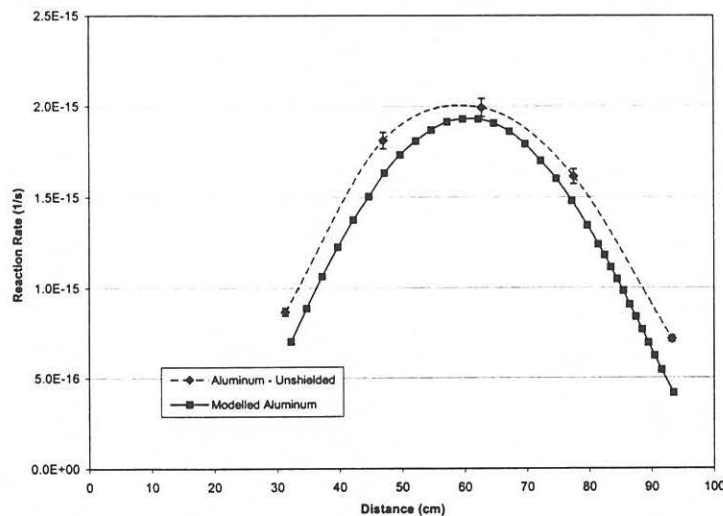


Figure 11: Core 48I Axial Reaction Rates of Bare Al

Figures 10 and 11 are axial maps of reaction rates for aluminum and cobalt along Site 8d of Core 48I. The simulation is in good agreement with the experimental results from five cobalt/aluminum wires spaced along a sample tube. Distances were measured from the bottom of the model, with the bottom of the reactor's grid plate located at 10 cm.

Figures 12 through 15 show the axial distribution of cobalt and aluminum reaction rates in Sites 7c and 8f of Core 48M for both bare and cadmium lined RIFLS tubes. There is good spatial agreement between the simulation and experiment, but the peak activity occurs consistently about 2.25 cm higher up in the model of Site 7c than in the experiment. The modelled cobalt reaction rates in the four cases agree with the experiment. The simulated reaction rates of aluminum agree with experiment in three of the four cases, with most data points falling within experimental error.

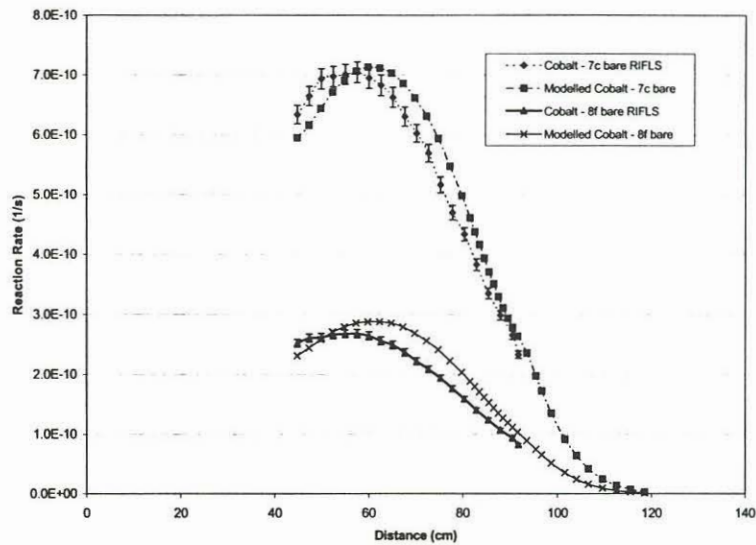


Figure 12: Axial Map of bare Cobalt Reaction Rates - Core 48M

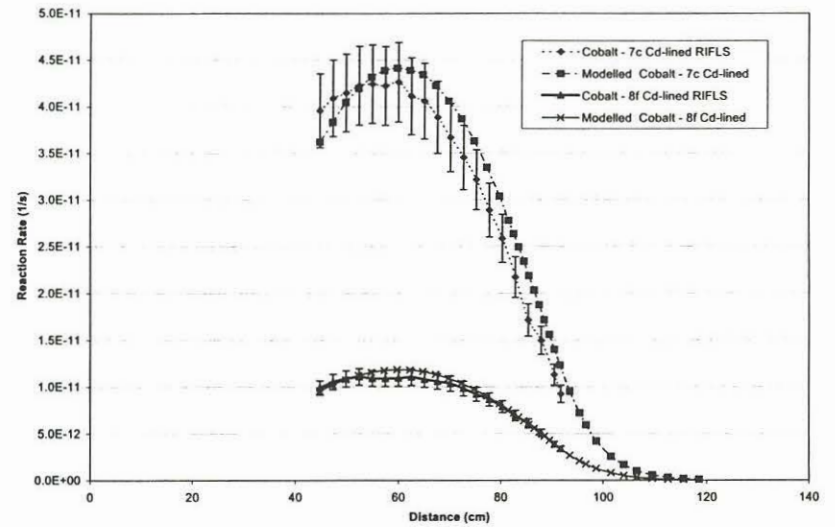


Figure 13: Axial Map of Cd-Covered Cobalt Reaction Rates - Core 48M

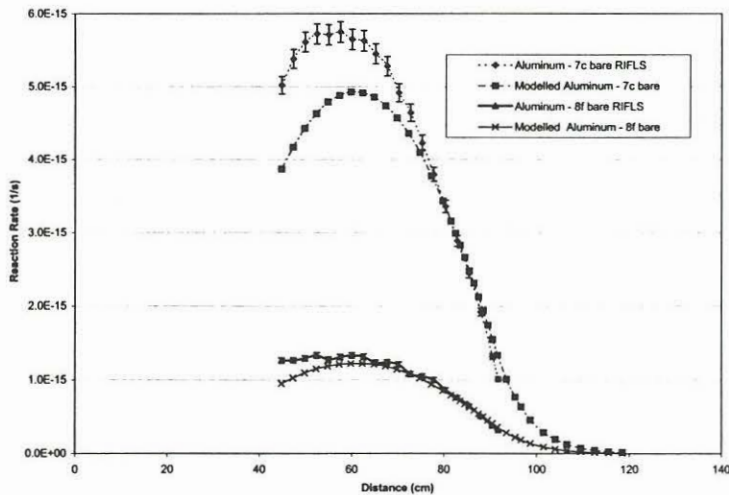


Figure 14: Axial Map of bare Aluminum Reaction Rates - Core 48M

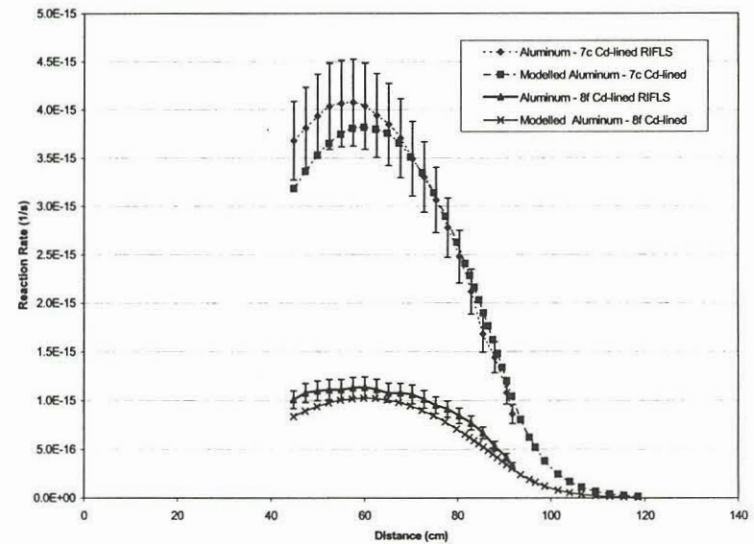


Figure 15: Axial Map of Cd-covered Aluminum Reaction Rates - Core 48M

Maps of Core 49A Sites 7c and 7f gave similar results. However, there was some indication that the cobalt/aluminum “cages” were not properly placed at the bottom of the RIFLS tubes.

6.0 Neutron Flux Estimates in MNR

The SAND-II spectral unfolding code was used to generate flux spectra from the experimental reaction rates. As an input spectrum, a Maxwell-Boltzmann distribution with an average neutron temperature of 590 K was used for most of the thermal range and a 1/E dependence for the range 0.38 eV to 255 keV.⁽¹⁰⁾ For the fast neutrons, an empirically derived formula for ²³⁵U fission was used: the Watt distribution.⁽¹¹⁾ The results are sensitive to shape of

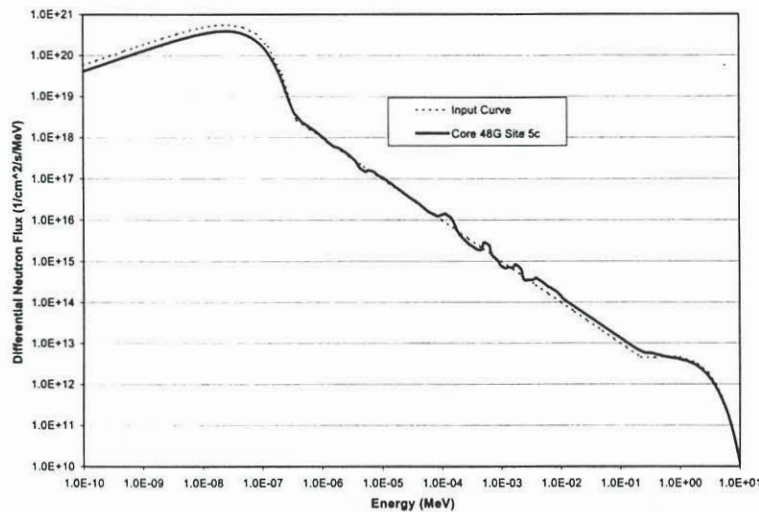


Figure 16: Differential Neutron Flux per MeV vs. Energy for SAND-II Input and Core 48G Site 5c Output

the input flux spectrum, so the boundaries of the 1/E dependence were chosen so that the SAND-II outputs most closely matched the experimental reaction rates.

Figure 16 shows the differential neutron flux spectrum input and output for Core 48G Site 5c, based on 620 energy intervals. The flux is per MeV. These can be integrated over the same 8 energy groups as the model. Figures 17 and 18 compare the SAND-II unfolded spectra with those generated by the model and show good agreement.

7.0 Limits to Flux Estimation by a Model

There are limits to how well experimental data can confirm the neutron flux spectra generated by a model.

In cases where reaction rates are the same, this does not mean that the model is a good representation of the true reactor flux spectrum. Since each nuclear reaction occurs over a spectrum of neutron flux energies, different flux spectra could give rise to the same reaction rate for a given foil. This would be true, for example, if a model overestimated an average cross section in one energy group, and underestimated it in another. Or even if the cross sections were accurate, a model may overestimate a resonance reaction and underestimate a thermal reaction and still give rise to a reaction rate that is the same as the experimentally determined value.

In most cases virtually all the reaction for each sample occurs in just one of the eight energy groups modelled. If the reaction rate is the same as a well determined experimental value, the flux for the group would be well known, to within the error of the cross section. However, little would be known about the flux in the remaining 7 groups for that sample.

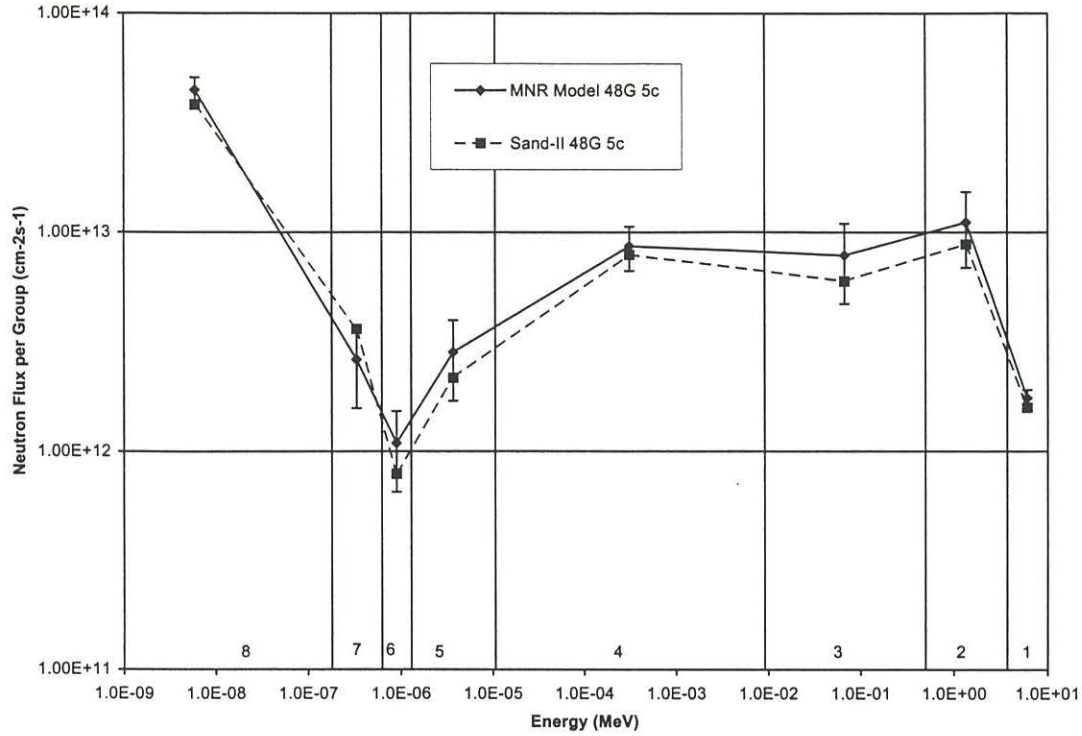


Figure 17: Neutron Flux vs. Energy Group for Core 48G Site 5c Modelled and SAND-II

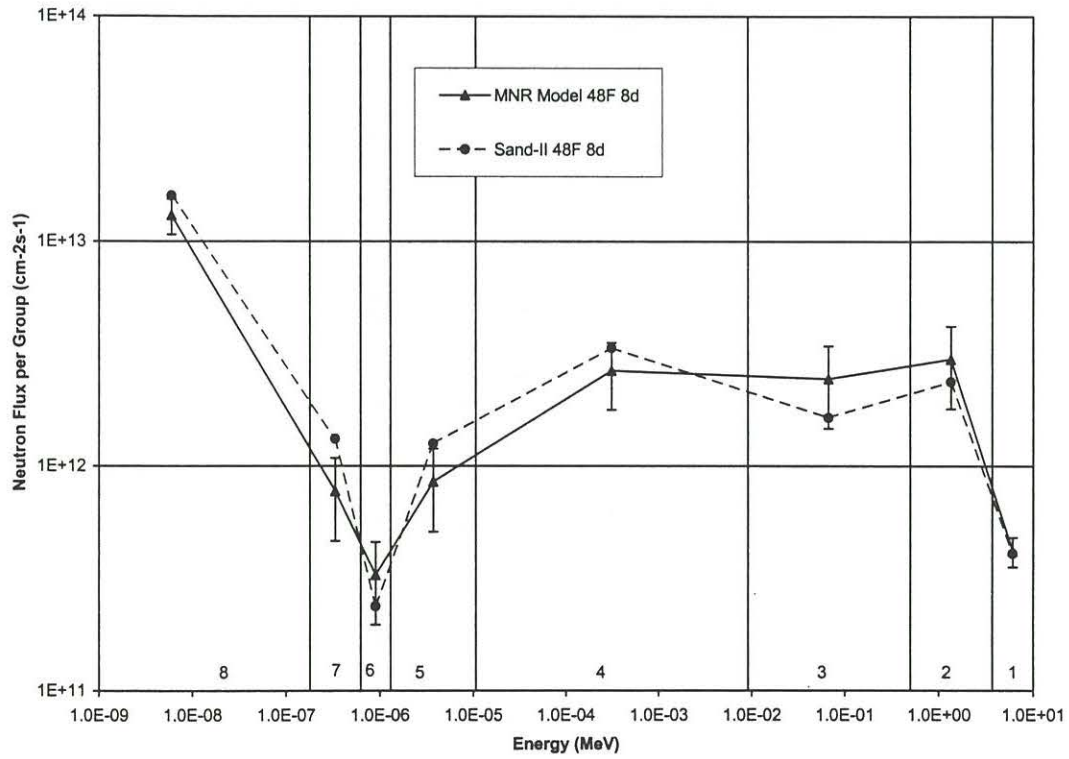


Figure 18: Neutron Flux vs. Energy Group for Core 48G Site 5c Modelled and SAND-II

The actual reaction rate (R_s'') for a foil in the reactor can be expressed as an integration of the product of the actual differential flux $\phi''(E)$ and the actual energy dependent cross section $\sigma''(E)$. The integration can be written as:

$$R_s'' = \int \sigma''(E)\phi''(E)dE \quad (9)$$

With no loss in accuracy, the integral could be split up over i energy groupings.

The computed reaction rate is a numerical integration of the product of the average group cross section (σ_i) and the integrated flux (ϕ_i) over the number of groups (N). This reaction rate is:

$$R_s = \sum_{i=1}^N \sigma_i \phi_i \quad (10)$$

If the k^{th} term is removed from the sum in Equation 10, the flux in the k^{th} group could be written in terms of the others:

$$R_s = \sigma_k \phi_k + \sum_{g \neq k} \sigma_g \phi_g, \quad \phi_k = \frac{1}{\sigma_k} \left(\sum_{g \neq k} \sigma_g \phi_g - R_s \right) \quad (11)$$

It can be shown that there is a limit to the error in the flux of the k^{th} group which is dependent on how much reaction occurs in the other groups and how well the cross sections and fluxes in the other groups are known:

$$\varepsilon_{r\phi k} = \frac{(1 + \varepsilon_{rR_s} \pm \varepsilon_{rR_s''})}{(1 + \varepsilon_{r\sigma k})} \left[1 + \sum_{g \neq k} \left(\frac{R_{sg}}{R_{sk}} \right) \left(1 - \frac{(1 + \varepsilon_{rR_s} \pm \varepsilon_{rR_s''})}{(1 + \varepsilon_{r\sigma g})(1 + \varepsilon_{r\phi g})} \right) \right]^{-1} - 1 \quad (12)$$

where: $\varepsilon_{r\phi k}$ = the relative difference between computed and actual fluxes for the k^{th} energy group

ε_{rR_s} = the relative difference between computed and actual reaction rates

$\varepsilon_{rR_s''}$ = the relative experimental error in the actual reaction rate

$\varepsilon_{r\phi k}$ = the relative difference between neutron fluxes for the k^{th} energy group

$\varepsilon_{r\phi g}$ = the relative difference between fluxes for the g^{th} energy group such that $g \neq k$

$\varepsilon_{r\sigma k}$ = the relative difference between average cross sections for the k^{th} energy group

$\varepsilon_{r\sigma g}$ = the relative difference between average cross sections for the g^{th} energy group, such that $g \neq k$

R_s = the computed reaction rate for the foil

R_{sk} = the computed reaction rate due to flux in the k^{th} energy group

R_{sg} = the computed reaction rate due to flux in the g^{th} energy group, $g \neq k$

Equation 12 was applied to Core 48G Site 5c to provide a limit to the error in the flux estimate. The aluminum foil results can estimate the flux of Group 1 to within 9 %. The indium foil (fast reaction) can estimate the flux in Group 2 to within 38 %. The cobalt foil can estimate flux in Groups 4 and 8 to within 23 % and 14 % respectively. In Site 8d of Core 48F, the experimental results of the iron foil gave a slightly more accurate determination of the Group 8 flux than the cobalt foil (a maximum deviation of 18 % compared to 19 %). These estimates require two assumptions: that the errors in the foils' microscopic cross sections are less than 5 % for any energy group; and the calculated flux in any other group is not more than 40 % off the actual value.

In Figures 17 and 18, the SAND-II unfolded spectra fall within or very close to these error ranges, except for Group 7 in core 48F site 8d. The most well determined fluxes are in

Groups 1, 4, and 8, and there is agreement between MNR model and the SAND-II code in those three groups.

Equation 12 can also be used to show that cadmium-shielded gold foils are the most likely to provide useful information on Group 5 and that there is little accurate information provided by any foil about the neutron flux in energy Group 3 (9.1 keV to 498 keV) and Groups 6 and 7 (0.18 eV to 1.3 eV).

Conclusions

Good agreement between experimental and calculated reaction rates were found in the majority of cases. The CoAl wire results along the axes of two sites showed good spatial agreement between the experiment and model.

In MNR, the most useful foils for confirming simulated neutron flux estimates were aluminum (3.68 to 10.0 MeV), indium fast reaction (0.498 to 3.68 MeV), cadmium-covered cobalt (10.68 eV to 9.12 keV), gold (1.30 to 10.68 eV), and cobalt or iron (0.0002 to 0.18 eV). The neutron flux in energy ranges 9.1 keV to 498 keV and 0.18 eV to 1.3 eV are difficult to determine by any foil.

In the most well determined energy groups, there is good agreement between the neutron flux spectra of the MNR model and the SAND-II spectral unfolding code.

References

1. Griffiths, J., "WIMS-AECL Users Manual", AECL RC-1176, COG-94-52, March 1994.
2. Vigil, J.C., "3DDT, A Three Dimensional Multigroup Diffusion-Burnup Program", LA43-4396, UC-32 Mathematics and Computers, TID-4500, September 1970, Argonne Code Center Abstract 463.
3. SAND-II/PC, Lahey Fortran F77EM/32 Version, Radiation Shielding Information Center, Oak Ridge National Laboratory, 1993.
4. American Society for Testing and Materials, "Method for Determining Neutron Flux, Fluence, and Spectra by Radioactivation Techniques - E261-77", *1989 Annual Book of ASTM Standards*, Vol. 12.02, 1989, pp. 56-64.
5. American Society for Testing and Materials, "Standard Method for Determining Neutron Reaction and Fluence Rates by Radioactivation Techniques - E262-86", *1989 Annual Book of ASTM Standards*, Vol. 12.02, 1989, pp. 56-73.
6. McElroy, W.N., *et al.*, *Documentation for CCC-112/SAND II Code Package*, Radiation Shielding Information Center, Oak Ridge National Laboratory, July, 1980.
7. Day, S.E., "MNR Core Component Technical Specifications - MNR Technical Report 98-01", Unpublished Report, McMaster Nuclear Reactor, October 1, 1998.
8. Aptec Engineering Ltd., "PCMCA/WIN - PC Based MCA Installation and Operations Manual", Unpublished Report, Version 4.00, October 1989.
9. Knoll, Glenn F., *Radiation Detection and Measurement*, John Wiley and Sons Inc., 1979.
10. Duderstadt, James J., and Louis J. Hamilton, *Nuclear Reactor Analysis*, John Wiley and Sons, 1976.
11. Watt, B.E., "Energy Spectrum of Neutrons from Thermal Fission of U^{235} ", *Physical Review*, Vol. 87 No. 6, September 1952, pp. 1037-1041.